Design of Polarization Conversion Metasurfaces with Low-Scattering Multi-Beam and Multi-Polarization

Original
Design of Polarization Conversion Metasurfaces with Low-Scattering Multi-Beam and Multi-Polarization / Mao, X., Wang, J., Zhang, Z., Li, Z., Li, Y.. - In: IEEE ANTENNAS AND WIRELESS PROPAGATION LETTERS. - ISSN 1536-1225. - (2026), pp. 1-5. [10.1109/lawp.2026.3697208]

Publisher:
IEEE

Published
DOI:10.1109/lawp.2026.3697208

This article has been accepted for publication in IEEE Antennas and Wireless Propagation Letters. This is the author's version which has not been fully edited and content may change prior to final publication. Citation information: DOI 10.1109/LAWP.2026.3697208

Design of Polarization Conversion Metasurfaces with Low-Scattering Multi-Beam and Multi-Polarization

Xinhua Mao, Junhong Wang, *Senior Member, IEEE*, Zhan Zhang, *Member, IEEE*, Zhaohua Li, *Student Member, IEEE* and Yujian Li, *Member, IEEE*

***Abstract*—This paper proposes two types of phase gradient metasurfaces, named as non-centrosymmetric beam metasurface (NCSM) and centrosymmetric beam metasurface (CSM), which exhibit remarkable performance in reducing radar cross-section (RCS). For the NCSM, when a circularly polarized (CP) wave is incident, it scatters incident wave into 45 beams accompanied by polarization conversion. When a linearly polarized (LP) wave is incident, the NCSM can generate total of 90 beams, including 45 left-circularly polarized (LCP) beams and 45 right-circularly polarized (RCP) beams. In contrast, when either CP or LP waves are incident on a CSM, it scatters incident wave into 36 beams and simultaneously achieves polarization conversion. The NCSM achieves over 10 dB multi-polarization RCS reduction across frequency range from 14.3 GHz to 33.4 GHz (80.1% relative bandwidth). Similarly, the CSM achieves over 10 dB multi-polarization RCS reduction within a frequency range from 14.9 GHz to 33.5 GHz (76.8% relative bandwidth). The proposed metasurfaces provide an efficient way to achieve multi-polarization RCS reduction, which can be adapted to the complex radar detection environment.**

***Index Terms*—Metasurface, multi-polarization, gradient phase superposition, polarization conversion metasurface (PCM), RCS reduction.**

I. INTRODUCTION

With the development of stealth technology and its application, research on radar cross-section (RCS) reduction has garnered significant attention [1],[2]. Available RCS reduction methods can be primarily categorized into following aspects: shaping optimization [3], polarization conversion [4]-[6], absorbers [7]-[11], frequency selective surfaces (FSS) [12], [13], artificial magnetic conductors (AMC) [14]-[16], and coded metasurfaces [17]-[21]. Among them, polarization conversion technology has received extensive attention due to its capability of achieving polarization stealth. Because the bistatic scattering performance realized by single polarization conversion is not as good as expected, so many studies combine polarization conversion with other methods to achieve better stealth performance. For instance, reference [22] proposes an aperiodic sunflower-like phase arrangement combined with polarization conversion to achieve scattering reduction of circularly polarized (CP) wave. Reference [23] proposes chessboard polarization conversion metasurface (PCM) to achieve 10 dB monostatic RCS reduction of linearly polarized (LP) wave across frequency band from 5.5 GHz to 37 GHz. The PCMs proposed in references [24] to [26] achieve RCS reduction for LP waves, but do not address that these designs would also produce similar RCS reduction effects for CP waves. The multilayer metasurface proposed in reference [27] achieves RCS reduction for both CP and LP waves, with a -7 dB relative bandwidth of 88.3%. Reference [28] proposes a 1-bit encoded PCM that achieves polarization conversion and scattering reduction of LP from 5.56 GHz to 19.07 GHz, but does not involve discussion on the case of CP wave. The 1-bit PCM proposed in reference [29] achieves only 16 scattering beams of LP and CP waves across frequency band from 4.1 GHz to 17 GHz, but limited number of the bistatic beams constrains its effectiveness. References [30], [31] and [32] propose programmable harmonic and wavefront control methods, but are focused mainly on single-polarized waves. In overall, most available studies are focused on stealth problem of single-polarized waves. Therefore, designing multi-polarization compatible and multi-beam controllable PCM is critical important for achieving multi-polarization stealth performance.

The metasurfaces proposed in this paper integrate phase gradient metasurface with PCM using the principle of phase superposition, achieving wideband multi-polarization stealth characteristics. The structural design and reflection characteristics of the metasurface units are given in Section II. In Section III, two distinct metasurfaces are designed, and their multipolarization performances are evaluated. Section IV presents the fabrication and measurement of both metasurface types, along with discussion of experimental results. Finally, conclusions are drawn in Section V.

II. STRUCTURE AND ANALYSIS OF UNIT CELL

The unit cell of the proposed metasurface consists of three layers, as shown in Fig. 1, the upper layer is a copper pattern, the middle layer is a dielectric substrate with a permittivity of 2.2, and the bottom layer is a metal plate acting as a ground

---

This work was supported by the National Natural Science Foundation of China under Grant U2241204, U2541209. (Corresponding author: Junhong Wang) The authors are with the Key Laboratory of All Optical Network and Advanced Telecommunication Network, Ministry of Education, Institute of Light wave Technology, Beijing Jiaotong University, Beijing 100044, China. (e-mail: wangjunh@bjtu.edu.cn).

This article has been accepted for publication in IEEE Antennas and Wireless Propagation Letters. This is the author's version which has not been fully edited and content may change prior to final publication. Citation information: DOI 10.1109/LAWP.2026.3697208

reflector. The unique plum blossom structures in upper layer increase the bandwidth, while the stripes connected with them realize the polarization conversion function. The final optimized structural parameters are: p = 4.8 mm, t = 0.035 mm, h = 2 mm, l = 2.35 mm, w = 0.5 mm, d = 1.08 mm. The reflection characteristics of the unit cell are simulated by full wave method using periodic boundary conditions, and the scattering performances are presented in Fig. 2. Fig. 2(a) shows the cases of unit cells with $\alpha = 45°$ and $\alpha = 135°$ for a CP plane wave incident from -z direction, the bandwith for polarization conversion ratio (PCR) larger than 95% is 85% (13.8 - 34.2 GHz). Fig. 2(b) further presents the cases of two unit cells for LP incident wave, and the bandwidth for PCR larger than 95% is 76.9% (14.9 - 33.5 GHz).

According to Pancharatnam-Berry (PB) phase theory, the phase of co-polarization reflected wave depends on the rotation angle of copper pattern in upper layer [33]. For a CP wave incident, when the pattern rotates α, the phase change of co-polarization reflection coefficient is $\alpha_{\text{co-pol}} = \pm 2\alpha$, where ± represent the left or right circularly polarized waves. Fig. 3 presents the reflection phases for both CP and LP plane waves under normal incidence. As shown in Fig. 3(a), the co-polarized phase shifts by 360° as α rotates from 0° to 180°, demonstrating flexibility of phase control through structural rotation. As can be seen from Fig. 3(b), when the rotation angle α is set to 45° or 135°, the phase of cross-polarized wave shifts by 180°. When the patch is oriented at 45° relative to the x-axis, it induces asymmetric scattering for x- and y-polarized waves, thereby converting incident LP plane waves into cross-polarized waves.

According to the generalized Snell's law [34], when an electromagnetic wave is incident on a metasurface, to obtain a reflected wave propagating in direction of (θ, φ), the reflection phase in a unit cell aperture at (x, y) on the metasurface should satisfy:

$$\phi_r(x,y) = k_r \sin(\theta)\cos(\varphi)x + k_r \sin(\theta)\sin(\varphi)y \qquad (1)$$

where k_r is the free space wave number of the reflected wave. When the unit-cell reflection coefficient amplitude approaches unity in the working frequency range, the scattering performance is mainly dominated by the phase, with each phase gradient distribution generating a specific scattering direction. Therefore, the superposition of multiple phase gradient distributions will generate multiple beams in the far field, and redistributing the energy in space. The superposed phase distribution is [35]:

$$\phi_{total}(x,y) = \arg \sum_{k=1}^{m} e^{j\phi_{rk}(x,y)} \qquad (2)$$

Accordingly, the beam directions of multiple reflection beams can be designed based on Equation (2).

III. DESIGN AND ANALYSIS OF MULTI-POLARIZATION MULTI-BEAM LOW-SCATTERING METASURFACES

A. Design of non-centrosymmetric beam metasurface (NCSM)

Based on Equation (2), multi-beam scattering control of incident LCP waves is achieved using the principle of phase gradient superposition, and three multilayer beam-superposition metasurfaces with 45 beams, 60 beams and 75 beams are designed. The three metasurfaces are designed to be non-centrosymmetric (NCSM), meaning that none of the scattered beams has a centrosymmetrically corresponding counterpart. Fig. 4(a) presents the phase distributions of the three NCSMs, which are composed of multiple phase profiles, while Fig. 4(b) illustrates their bistatic scattering patterns under LCP wave incidence. It can be observed that as the number of beams increases, the bistatic RCS reduction performance gradually improves.

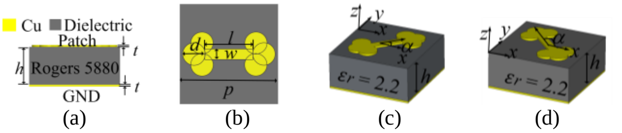

(a) (b) (c) (d)

Fig. 1 Unit cell structure, (a) side view, (b) top view, (c) 3D view, α = 45°, (d) 3D view, α = 135°.

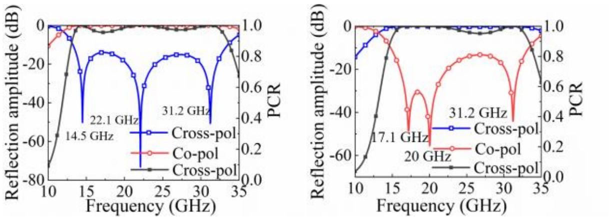

(a) (b)

Fig. 2 Reflection characteristics and PCR of reflection wave of the unit cell, (a) CP plane wave incident from normal direction, (b) LP plane wave incident from normal direction.

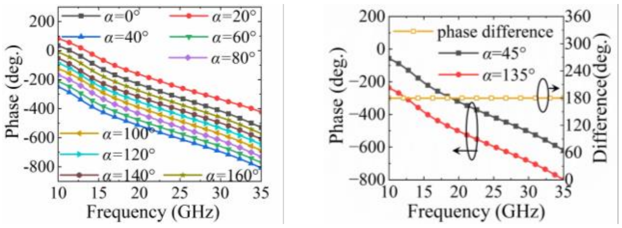

(a) (b)

Fig. 3. Phase of reflection wave when plane wave is incident from normal direction, (a) phase of co-polarized wave as function of frequency and rotation angle φ for CP wave incident, (b) phase of cross-polarized wave as function of frequency when rotation angle φ equals to 45° and 135° for LP wave incident.

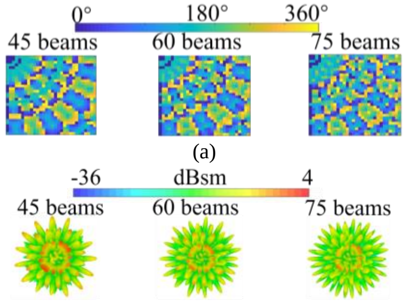

(a)

(b)

Fig. 4. Phases of the 45-beam NCSM, 60-beam NCSM, and 75-beam NCSM, along with their simulated bistatic scattering patterns under LCP normal incident, (a) phases, (b) simulated bistatic scattering patterns. The 45 beams are composited by 15 beams at θ = 15° (φ: 0°-336°, $\Delta\varphi$ = 24°), 15 beams at θ = 30° (φ: 12°-348°, $\Delta\varphi$ = 24°) and 15 beams at θ = 45° (φ: 0°-336°, $\Delta\varphi$ = 24°). The 60 beams are composited by the above 45 beams and additional 15 beams at θ = 60° (φ: 12°-348°, $\Delta\varphi$ = 24°). The 75 beams are composed by the 60 beams and additional 15 beams at θ = 75° (φ: 0°-336°, $\Delta\varphi$ = 24°).

This article has been accepted for publication in IEEE Antennas and Wireless Propagation Letters. This is the author's version which has not been fully edited and content may change prior to final publication. Citation information: DOI 10.1109/LAWP.2026.3697208

Fig. 5(a) shows the monostatic RCSs of the three NCSMs for normal incidence. The 60-beam NCSMs, due to additional beams desiged at large θ angles, increase the system's sensitivity to amplitude and phase errors, thereby reducing the maximum reduction in monostatic RCS and compressing the effective bandwidth. The results indicate that the 45-beam NCSM has widest bandwidth and achieves greatest RCS reduction at the center frequency. Therefore, the 45-beam NCSM is designed based on the PB-phase principle, with its co-polarized phase satisfying $\varphi_{\text{co-pol}} = \pm 2\alpha$, enabling conjugate phase modulation for LCP and RCP waves [35]. This modulation deflects the incident LCP wave to direction (θ, φ_0) and incident RCP wave to direction (θ, $\varphi_0+\pi$), forming a pair of centrally symmetric beams. This phase antisymmetry allows symmetric beam control for orthogonal CP waves and provides the foundation for LP regulation, as an LP wave can be equivalently described as the superposition of two equal-amplitude, in-phase LCP and RCP waves [36], [37].

Fig. 6 shows bistatic RCS of the 45-beam NCSM under *x*-polarized wave normal incidence. The LCP component of incident wave is scattered into 45 LCP beams along the pre-designed directions, while the RCP component is scattered into another 45 RCP beams along the corresponding centrosymmetric directions. Compared with LCP incident case in Fig. 4(b), LP wave excitation can generate a total of 90 scattered beams, enhancing the bistatic scattering reduction performance. In Fig. 5(b), the NCSM achieves monostatic RCS reduction over 10 dB from 14 to 34 GHz under both CP and LP normal incidence, about 83.3% relative bandwidth. These results confirm stealth performance of the metasurface against LP detection.

The 45-beam NCSM is examined for its anti-detection performance under unknown polarizations and incident angles. For normal incident CP waves, due to its rotational symmetry, the NCSM generates a stable RCS distribution over the angle range φ. Fig. 7(a) illustrates the response of NCSM under normal incidence of LP waves, where the RCS reduction remains almost constant as φ varies. Under oblique incidence as shown in Fig. 7(b) and Fig. 7(c), the NCSM maintains an RCS reduction greater than 6 dB for both LP and CP waves at θ = 60°, and increases over 10 dB at θ = 35°. At large incident angles, coupling variations and reduced PCR introduce phase and amplitude deviations, thereby weakening scattering control. In this case, wide-angle performance can be improved through multi-angle joint optimization, angle-robust meta-atom design, and introducing additional degrees of freedom such as multilayer structures.

B. *Design of centrosymmetric beam metasurface (CSM)*

The analysis of NCSM in previous section (Fig. 4(a)) reveals that the metasurface units possess diverse phase distributions. However, if generating centrosymmetric beams, the phase states of metasurface units will be simplified to only 0 and π, thereby improving the coding efficiency. This section will systematically analyze the performance of centrosymmetric-beam metasurfaces (CSM).

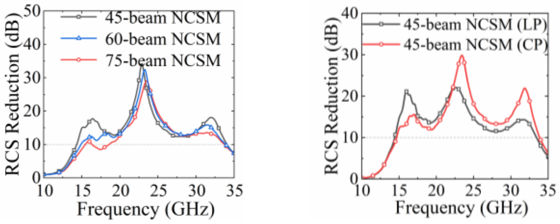

(a) (b)

Fig. 5. Monostatic RCSs of the NCSMs under normal incident, (a) 45, 60 and 75 beam NCSMs, CP wave incident, (b) 45-beam NCSM, CP/LP wave incident

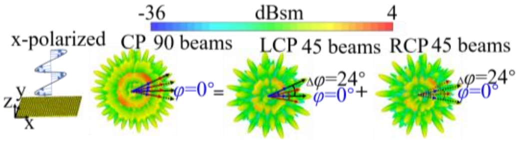

Fig. 6. Simulation results of scattering characteristics of the 45-beam NCSM for *x*-polarized plane wave incident normally.

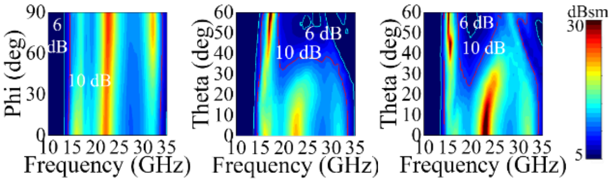

(a) (b) (c)

Fig. 7. Simulation monostatic results of RCS reduction of the 45-beam NCSM, (a) LP plane wave incident normally at different φ, (b) LP plane wave incident at different θ, (c) CP plane wave incident at different θ.

Using multi-layer beam superposition approach, two CSMs with 36-beam and 54-beam are developed. Each beam has a corresponding centrally symmetric counterpart. Fig. 8 shows the phase distributions and bistatic scattering patterns under normal LCP incidence, demonstrating cross-polarization conversion while scattering in predetermined directions. Fig. 9(a) shows that the 36-beam CSM outperforms the 54-beam CSM in RCS reduction depth, so the 36-beam CSM is selected for further study. To investigate multi-polarization stealth performance, Fig. 10 presents scattering behavior of the 36-beam CSM under normal incidence of *x*-polarized wave. Due to geometric phase antisymmetry and centrosymmetric beam design, the scattered LCP and RCP beams exhibit a 180° phase difference and a symmetric distribution, ultimately generating 36 *y*-polarized beams. In Fig. 9(b), the CSM achieves monostatic RCS reduction larger than 10 dB from 14.9 to 33.5 GHz (76.8% bandwidth) under CP/LP normal incidence. Fig. 11 further characterizes the 36-beam CSM under different polarizations and oblique incidence. Although the performance under oblique incidence is comparable to that of NCSM, as shown in Fig. 11(b) and Fig. 11(c), the LP wave RCS reduction varies obviously with φ (shown in Fig. 11(a)), peaking at φ = 0°/90° and declining after 45°, attributed to amplitude/phase shifts that degrade scattering control stability. These results confirm the effective CP/LP conversion capability of CSM for multipolarization stealth. The NCSM offers superior polarization angle φ stability and good θ angular robustness, but shows higher coding complexity, needs strict fabrication precision, and supports only CP wave conversion, making it only suitable for high-precision cases with stringent bistatic requirements and unknown incident angles. In contrast, CSM provides good θ angular robustness, simpler coding, lower cost, and supports both LP and CP conversion, though it

This article has been accepted for publication in IEEE Antennas and Wireless Propagation Letters. This is the author's version which has not been fully edited and content may change prior to final publication. Citation information: DOI 10.1109/LAWP.2026.3697208

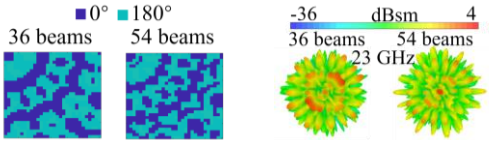

(a) (b)

Fig. 8. Phases of the 36 beams CSM and 54 beams CSM, along with their simulated bistatic scattering patterns, (a) phases, (b) simulated bistatic scattering patterns. The 36 beams are composed by 18 beams at $\theta = 15^\circ$ (φ: 0°~340°, $\Delta\varphi = 20^\circ$) and 18 beams at $\theta = 30^\circ$ (φ: 0°~340°, $\Delta\varphi = 20^\circ$). The 54 beams are extended by the 36 beams through adding additional 18 beams at $\theta = 45^\circ$ (φ: 0°~340°, $\Delta\varphi = 20^\circ$).

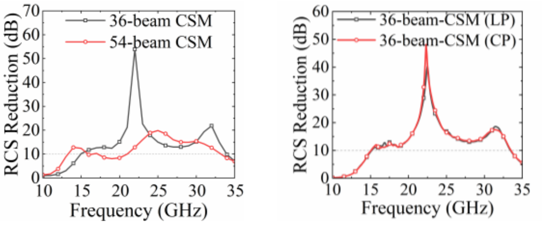

(a) (b)

Fig. 9. Simulated monostatic RCSs of the CSMs, (a) 36-beam and 54-beam CSMs, CP wave normal incidence, (b) 36-beam CSM, CP/LP wave normal incidence.

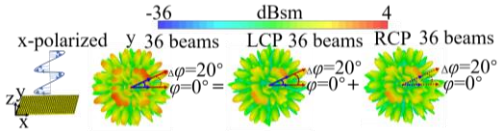

Fig. 10. Simulation results of scattering characteristics of the 36-beam CSM for *x*-polarized plane wave incidence.

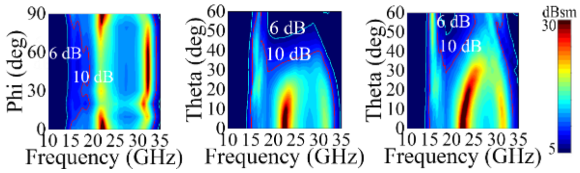

(a) (b) (c)

Fig. 11. Simulation monostatic RCS reduction of the 36-beam CSM, (a) LP plane wave incident at different φ, (b) LP plane wave incident at different θ, (c) CP plane wave incident at different θ.

is sensitive to polarization angle φ, making it more appropriate for low-cost applications demanding high polarization conversion performance.

IV. EXPERIMENT AND VERIFICATION

The 45-beam NCSM and 36-beam CSM are fabricated and measured, the samples and test environment are illustrated in Fig. 12. The measured monostatic RCSs of the two metasurfaces under CP/LP wave incidence are shown in Fig. 13(a) and Fig. 13(b), which are in consistent with the simulation results. When a CP wave is incident on NCSM, bistatic scattering beams will appear at $\theta = 15^\circ$, $\theta = 45^\circ$ and $\theta = -30^\circ$ as shown in Fig .13(c) and Fig. 13(d), which is expected. When an LP wave is incident, centrally symmetric beams also appear, verifying the multipolarization characteristics of the NCSM. When CP and LP waves are incident on CSM, the bistatic scattering beams are measured using cross-polarized antenna at $\theta = 15^\circ$, $\theta = 30^\circ$, $\theta = -15^\circ$ and $\theta = -30^\circ$ as shown in Fig. 13(e) and Fig. 13(f), verifying the polarization conversion characteristics of the CSM. The simulated and measured monostatic RCSs under normal incidence are in good agreement, whereas the bistatic measurements exhibit beam broadening and deviations due to manufacturing tolerances, finite-size effects, near-field testing conditions, and the non-ideal plane-wave characteristics of the horn antennas. Despite these factors, the main lobe directions still coincide with the designed angles, thereby confirming the effectiveness of the beam superposition method.

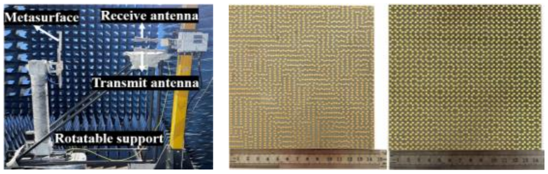

(a) (b) (c)

Fig. 12 Fabricated metasurfaces and measurement scenarios, (a) scenarios of RCS measurement in anechoic chamber, (b) 45-beam NCSM, (c) 36 beam CSM.

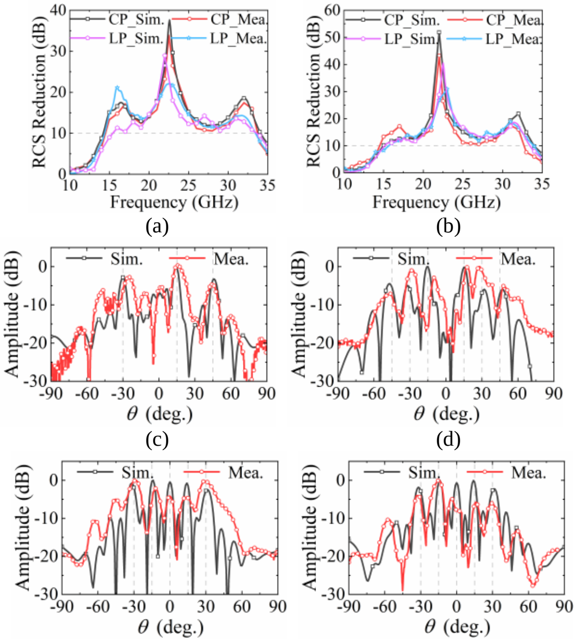

Fig. 13. Simulated and measured RCSs of the NCSM and CSM, (a) NCSM monostatic RCS, (b) CSM monostatic RCS, (c) NCSM E-plane bistatic pattern at 23 GHz, CP normal incidence, (d) NCSM E-plane bistatic pattern at 23 GHz, LP normal incidence, (e) CSM E-plane bistatic pattern at 23 GHz, CP normal incidence, (f) CSM E-plane bistatic pattern at 23 GHz, LP normal incidence.

V. CONCLUSION

This work presents a design framework for phase-gradient superposition metasurface, and designs two kinds phase-gradient superposed metasurfaces which exhibit multi-beam scattering, broadband low RCS and high cross-polarized conversion ratio for LP/CP waves. Experimental results show that Pancharatnam-Berry phase metasurfaces with rotationally symmetric unit cells can produce centrosymmetric beam deflections under LCP/RCP incidence, allowing scattering characteristices of LP multi-beam to be inferred and supporting multipolarization multi-beam stealth.

This article has been accepted for publication in IEEE Antennas and Wireless Propagation Letters. This is the author's version which has not been fully edited and content may change prior to final publication. Citation information: DOI 10.1109/LAWP.2026.3697208

REFERENCES

[1] X. Gong, and X. Wan, “Automatic target recognition based on RCS and angular diversity for multistatic passive radar,” *IEEE Trans. Aerosp. Electron. Syst.*, vol. 58, no. 5, pp. 4226–4240, Oct. 2022.

[2] J. Palmer, D. Cristallini, and H. Kuschel, “Opportunities and current drivers for passive radar research,” *in Proc. IEEE Radar Conf.*, pp. 145-150, Oct. 2015.

[3] A. Muniyasamy and K. Rajakani, “UWB radar cross section reduction in a compact antipodal Vivaldi antenna,” AEU Int. J. Electron. Commun., vol. 99, pp. 369-375, Feb. 2019.

[4] Y. Liu, K. Li, Y. Jia, Y. Hao, S. Gong, and Y. J. Guo, “Wideband RCS reduction of a slot array antenna using polarization conversion metasurfaces,” IEEE Trans. Antennas Propag., vol. 64, no. 1, pp. 326–331, Nov. 2016.

[5] G.-Y. Deng et al., “Ultrabroadband RCS reduction design by exploiting characteristic complementary polarization conversion metasurfaces,” IEEE Trans. Antennas Propag., vol. 70, no. 4, pp. 2904–2914, Apr. 2022.

[6] Y. Qi, B. Zhang, C. Liu, and X. Deng, “Ultra-broadband polarization conversion meta-surface and its application in polarization converter and RCS reduction,” IEEE Access, vol. 8, pp. 116675-116684, Jun. 2020.

[7] Y. Ma, J. Wang, L. Shi, et al., “Ultra-wideband, optically transparent, and flexible microwave metasurface absorber,” Optical Materials Express, vol. 11, no. 7, pp. 2206-2218, Jul. 2021.

[8] Min P, Song Z, Yang, et al., “Multispectral meta-film design: simultaneous realization of wideband microwave absorption, low infrared emissivity, and visible transparency,” Optics Express, vol. 30, no. 18, pp. 32317-32330, Aug. 2022.

[9] C. F. Fu, L. Zhang, L. J. Liu, S. H. Dong, W. J. Yu, and L. F. Han, “RCS reduction on patterned graphene-based transparent flexible metasurface absorber,” IEEE Trans. Antennas Propag., vol. 71, no. 2, pp. 2005–2010, Feb. 2023.

[10] Z. Song, P. Min, et al., “A bilateral coding metabsorber using characteristic mode analysis,” IEEE Antennas Wireless Propag. Lett., vol. 21, no. 6, pp. 1228-1232, Jun. 2022.

[11] Z. Li, J. Wang and W. Zheng, “Deformable transparent metasurface with multipolarization absorptive characteristics for RCS reduction,” IEEE Trans. Antennas Propag., vol. 73, no. 3, pp. 1768-1776, March 2025.

[12] W. J. Liao, W. Y. Zhang, Y. C. Hou, et al., “An FSS-integrated low-RCS radome design,” IEEE Antennas Wireless Propag. Lett., vol. 18, no. 10, pp. 2076-2080, Oct. 2019.

[13] Ghayekhloo A, Afsahi M, Orouji A A, “Checkerboard plasma electromagnetic surface for wideband and wide-angle bistatic radar cross section reduction,” IEEE Trans. Plasma Sci., vol. 45, no. 4, pp. 603-609, Apr. 2017.

[14] Xue J, Jiang W, Gong S, “Chessboard AMC surface based on quasi-fractal structure for wideband RCS reduction,” IEEE Antennas Wireless Propag. Lett., vol. 17, no. 2, pp. 201-204, Feb. 2018.

[15] Sang D, Chen Q, Ding L, et al, “Design of checkerboard AMC structure for wideband RCS reduction,” IEEE Trans. Antennas Propag., vol. 67, no. 4, pp. 2604-2612, Apr. 2019.

[16] Iriarte Galarregui, J. C., Tellechea Pereda, A., Martínez de Falcón, J. L., et al., “Broadband radar cross-Section reduction using AMC technology,” IEEE Trans. Antennas Propag., vol. 61, no. 12, pp. 6136-6143, Dec. 2013.

[17] Al-Nuaimi M K T, Huang G L, Whittow W G, et al，“Coding engineered reflector for wide-band RCS reduction under wide angle of incidence,” IEEE Trans. Antennas Propag., vol. 70, no. 10, pp. 9947-9952, Oct. 2022.

[18] Liu X, Gao J, Xu L, et al, “A coding diffuse metasurface for RCS reduction,” IEEE Antennas Wireless Propag. Lett., vol. 16, pp. 724-726, 2017.

[19] Y. Li, Q. Cao, and Y. Wang, “Radar cross section reduction metasurfaces based on phase gradient and chessboard structure,” *J. RF Microw. Comput. Aided Eng.*, vol. 28, no. 7, pp. e21457, 2018.

[20] F. Yuan, G. -M. Wang, H. -X. Xu, T. Cai, X. -J. Zou, and Z. -H. Pang, “Broadband RCS Reduction Based on Spiral-Coded Metasurface,” IEEE Antennas Wireless Propag. Lett., vol. 16, pp. 3188-3191, 2017.

[21] C. Fu, X. Zhang, X. Liu, et al., “RCS reduction of composite transparent flexible coding metasurface combined phase cancellation and absorption,” Opt. Express vol. 31, no. 17, pp. 27365-27380, 2023.

[22] Al-Nuaimi M K T, Hong W, Whittow W G, “Aperiodic sunflower-like metasurface for diffusive scattering and RCS reduction,” IEEE Antennas Wireless Propag. Lett., vol. 19, no. 7, pp. 1048-1052, Jul. 2020.

[23] Wang, Y., Xue, Q., Xie, H., Hu, Z., & Liao, S. “Bandwidth enhancement in arrow-shaped polarization conversion metasurface under seven plasmonic resonances,” IEEE Antennas Wireless Propag. Lett., vol. 23, no. 7, pp. 2254-2258, Jul. 2024.

[24] Q. Lina et al., “Broadband, polarization insensitive low-scattering metasurface based on lossy Pancharatnam-Berry phase particles,” Opt. Express, vol. 27, no. 15, pp. 21226-21238, 2019.

[25] J. Liu, J.-Y. Li, and Z. N. Chen, “Broadband polarization conversion metasurface for antenna RCS reduction,” IEEE Trans. Antennas Propag., vol. 70, no. 5, pp. 3834-3839, May 2022.

[26] Zhang, C., Cheng, J., Zhang, J., Cai, Q., Zhao, Y., Guo, S. and Shen, T., “Multi-Bit Coding Polarization Conversion Metasurface for RCS Reduction,” Microwave and Optical Technology Letters, vol. 67, no. 4, pp. e70199, Apr. 2025.

[27] H. X. Xu et al., “Deterministic approach to achieve broadband polarization-independent diffusive scatterings based on metasurfaces,” ACS Photonics, vol. 5, no. 5, pp. 1691-1702, Oct. 2017.

[28] Fu, H., Liu, N., Sheng, X. et al. “An optimized coding polarization conversion metasurface with a transmission window for RCS reduction,” Appl. Phys. vol. 131, no. 4, pp. 283, Mar. 2025.

[29] Geng W, Guo Q, Su J, et al. “Dartboard Metasurface for RCS Reduction and OAM Wave Generation,” IEEE Trans. Antennas Propag., vol. 73, no. 4, pp. 2497-2509, April 2025.

[30] H. W. Tian, X. G. Zhang, W. X. Jiang, X. Li, Y. K. Liu, C.-W. Qiu, T. J. Cui, “ Programmable controlling of multiple spatial harmonics via a nonlinearly phased grating metasurface,” Adv. Funct. Mater., vol. 32, no. 31, pp. 2203120, 2022.

[31] Tian, H.W., Xu, L., Li, X., Jiang, W.X. and Cui, T.J., “Integrated control of radiations and in-band co-polarized reflections by a single programmable metasurface,”. Adv. Funct. Mater., vol. 33, no. 36, pp. 2302753, 2023.

[32] Tian HW, Sun YL, Zhang XG, Li X, Zhu Q, Song C, Qiu CW, Cui TJ, Jiang WX. “Solar-powered light-modulated microwave programmable metasurface for sustainable wireless communications,” Nat. Commun., vol. 16, no. 1, pp. 2524, Mar. 2025.

[33] Arbabi, A., Horie, Y., Bagheri, M., & Faraon, A, “Dielectric metasurfaces for complete control of phase and polarization with subwavelength spatial resolution and high transmission,” Nature Nanotechnology, vol. 10, no.114, pp. 937-943, Aug. 2015.

[34] Sun S, He Q, Xiao S, et al, “Gradient-index metasurfaces as a bridge linking propagating waves and surface waves," Nature Materials, vol. 11, pp. 426-431, May 2012.

[35] J. Wang, J. Miao, Y. Yang and Y. Chen, "Scattering property and emissivity of a periodic pyramid array covered with absorbing material," IEEE Trans. Antennas Propag., vol. 56, no. 8, pp. 2656-2663, Aug. 2008.

[36] J. D. Kraus and R. J. Marhefka, Antennas for All Applications, 3rd ed. New York: McGraw-Hill, 2003.

[37] C. A. Balanis, Antenna Theory: Analysis and Design, 4th ed. Hoboken, NJ: John Wiley & Sons, 2016.